Electrochimica Acta 525 (2025) 146113

Contents lists available at ScienceDirect

Electrochimica Acta

journal homepage: www.journals.elsevier.com/electrochimica-acta

Unveiling the reversible sodium-ion storage mechanism in rutile TiO_2 nanorods

Angélica Duarte-Cárdenas [a], Liuda Mereacre [b], Michael Knapp [b], Pilar Díaz-Carrasco [a], Flaviano García-Alvarado [a], Alois Kuhn [a,*]

[a] Departamento de Química y Bioquímica, Facultad de Farmacia, Universidad San Pablo-CEU, CEU Universities, Urbanización Montepríncipe, 28668 Boadilla del Monte, Madrid, Spain
[b] Institute for Applied Materials (IAM), Karlsruhe Institute of Technology (KIT), Hermann-von-Helmholtz-Platz 1, D-76344 Eggenstein-Leopoldshafen, Germany

ARTICLE INFO

Keywords:
TiO_2
Rutile
Na-ion battery
Na-ion diffusion
Electrochemical sodium intercalation

ABSTRACT

Rutile titanium dioxide (TiO_2) is an abundant, cost-effective material with a one-dimensional ion diffusion pathway along the *c*-axis. However, its potential as an anode material for Na-ion batteries has been long underestimated due to its low electronic conductivity and restricted ion diffusion across the *ab*-plane. Despite its promising electrochemical properties, the origin of the electrochemical performances in TiO_2 rutile is still largely unclear. In this work, the Na^+storage mechanisms of TiO_2(R) nanorods, 50 nm in length and 5 nm in width, are systematically investigated. The overall charge storage in TiO_2 nanorutile is dominated by a mix of surface pseudo-capacitive and diffusion-control Na^+ intercalation, whose contributions strongly depend on the C-rate employed. Using *operando* X-ray diffraction, we demonstrate for the first time reversible Na^+ intercalation in the rutile tunnels at low C-rates, favored by the specific nanoarchitecture of TiO_2. In line with this, sodium diffusion coefficient is several orders of magnitude higher compared with previous reports (10^{-16} - 10^{-17} cm^2 s^{-1} vs. 10^{-20} cm^2 s^{-1}), ensuring a high reversible capacity of ~ 210 mAh g^{-1} at low 17 mA g^{-1} (C/20), and 140 mAh g^{-1} at 67 mA g^{-1} (C/5) with little capacity fade and improved cycling stability. Whereas high-rate capability of 71 mAh g^{-1} at 1.7 A g^{-1} is justified by the dominant pseudo-capacitive contribution to the total capacity at high cycling rates. Carbon-enriched TiO_2 (6.5:2.5:1) electrodes exhibit enhanced electrochemical sodium charge storage and kinetics, delivering a higher reversible capacity of 280 mAh g^{-1} at 17 mA g^{-1} and an improved high-rate capability of 128 mAh g^{-1} at 1.7 A g^{-1}. These results demonstrate the significant potential of TiO_2 nanorutile for high-rate sodium-ion battery applications.

1. Introduction

Titanium dioxide (TiO_2) has gained interest as a viable anode material for sodium-ion batteries (SIBs) due to its abundance, structural stability, and environmental friendliness. In addition, the theoretical capacity (336 mAh g^{-1}), comparable to hard carbon (150–430 mAh g^{-1}) [1–3], the stability and cycle life of TiO_2 have positioned it as a favorable option, especially for high-rate applications.

While various TiO_2 polymorphs have been investigated, rutile TiO_2 stands out for its thermal stability and unique sodium storage properties, despite its relatively low electronic conductivity. Interestingly, surface driven storage processes can enhance capacity retention and stability, making nanorutile TiO_2 particularly attractive for high-rate applications. Recent studies have shown that nanorods of rutile TiO_2 show higher performance as an anode material [4–6]. This improvement arises from the high surface area and short sodium diffusion paths associated with nanosized materials. In lithium systems, nanosizing TiO_2 increases both capacity and cycling stability, primarily due to capacitive or pseudo-capacitive processes that dominate at high rates. For SIBs, the limited ability to accommodate larger sodium ions within the structure with minimal volume changes is expected to favor surface charge storage mechanisms, which can be beneficial for long cycle life and mechanical stability.

Table 1 summarizes the results obtained from different studies on titanium dioxide materials with rutile structure used as electrodes in sodium batteries, including morphology, specific surface area (SSA), electrode composition and electrolyte used, working voltage range, applied current intensity, specific capacity after the first discharge and

* Corresponding author.
E-mail address: akuhn@ceu.es (A. Kuhn).

https://doi.org/10.1016/j.electacta.2025.146113
Received 14 December 2024; Received in revised form 22 March 2025; Accepted 24 March 2025
Available online 25 March 2025

reversible specific capacity after a given number of cycles [7–19].

Among the listed materials, C-TiO_2-RN (nanorutile) exhibits the highest initial discharge capacity (685.7 mAh g^{-1}) [8], while rutile TiO_2 mesocrystals and iron-doped rutile TiO_2 (cauliflower-like morphology) show excellent capacity retention of 283 mAh g^{-1} (after 100 cycles) [11] and 280 mAh g^{-1} (after 50 cycles) [13], respectively. The comparison underscores the strong influence of morphology, doping, and material composition on sodium storage properties, rate capability, and long-term cycling stability. However, although electrochemical performance of TiO_2 has been investigated in detail in some cases, a deeper understanding of the sodium storage mechanism and its influence on the rate performance is still needed. In addition, specific tailored nanoarchitectures can favor metal ion intercalation, boosting hereby capacity, as shown in our previous work on lithium intercalation in TiO_2 nanorods grown along the rutile tunnel *c* direction [20].

In this work, we investigate the electrochemical sodium storage properties of nanostructured TiO_2 rutile, derived from potassium bronze K_xTiO_2, as anode material for sodium ion batteries. The specific morphology of TiO_2 as nanorods and its surface properties facilitate both sodium ion diffusion and surface charge storage. A deeper understanding of the fundamental mechanisms of sodium-ion storage and diffusion in TiO_2 is achieved, emphasizing the contributions of both diffusion-controlled and pseudo-capacitive processes at various current densities supported by *operando* X-ray diffraction. Considering the insulating nature of TiO_2, the use of conductive carbon-enriched TiO_2 electrode compositions on high-rate capability and capacity retention is also investigated to assess its interest in developing high-performance SIBs.

2. Experimental section

2.1. Synthesis of TiO_2 rutile nanorods

Nanorutile titanium dioxide was synthesized using a two-step method. The first step involves the solid-state reaction of an intimate mixture of K_2CO_3 (Sigma-Aldrich) and TiO_2 (anatase) (Sigma-Aldrich, 99.8 %) at 950 °C for 10 h under a reducing Ar/H_2 (95:5) atmosphere, yielding the bronze with hollandite structure $K_{0.2}TiO_2$ (KTO) as the product. The resulting product is then subjected to oxidative extraction of $K^{\cdot}$. To facilitate K^+ extraction particle size of KTO bronze is first reduced by mechanically milling at 250 rpm for 1 hour using a planetary ball mill. Subsequently, in a typical oxidation 0.4 g of KTO bronze is mixed in a round-bottom flask with 1 mL of HNO_3:HCl (1:3 v/v), following the method reported by Pérez-Flores *et al.* [21] to achieve K extraction from hollandite KTO. Upon prolonged heating the mixture at 80 °C with vigorous stirring for 48 h, and six further additions of 1 mL HNO_3:HCl (1:3 v/v) aliquots the hollandite transforms into the rutile polymorph [20].

2.2. Physicochemical characterization

Structural characterization was carried out by X-ray diffraction on a Bruker D8 high-resolution diffractometer equipped with a LynxEye® position-sensitive solid-state fast detector (PSD) using Cu-Kα radiation ($\lambda\alpha1 = 1.5406$ Å, $\lambda\alpha2 = 1.54439$ Å).

The morphologies of TiO_2 nanorutile and the respective ex-situ and post-mortem electrodes were characterized by using scanning electron microscopy (SEM; Thermo Fisher Scientific Prisma E). Transmission electron microscopy (TEM) images and selected area electron diffraction (SAED) patterns were recorded by using a JEOL 3000F, JEOL 2100 JEM and a FEI Tecnai T20 G2 X-Twin 200 kV microscope.

Brunauer-Emmet-Teller (BET) specific surface area was measured by nitrogen sorption isotherms with a Micromeritics ASAP 2020 gas adsorption/desorption analyzer.

2.3. Electrochemical characterization

The electrochemical properties of TiO_2 were investigated using two electrode CR2032 coin-type cells, while three electrode Swagelok-type cells were used for electrochemical impedance spectroscopy (EIS) measurements.

The electrodes were prepared from two different mixtures composed of TiO_2 active material, Super C65 conductive carbon (Imerys, Timcal), and carboxymethyl cellulose (CMC, Merck) as a binder, homogenized and suspended in Milli-Q water at a ratio of 1 mL of solvent per 300 mg

Table 1
Electrochemical performance of various titanium dioxide-based anode materials.

Morphology	SSA / m^2 g^{-1}	Electrode and electrolyte composition	E / V	Current Intensity / C	Capacity 1st Cycle / mAh g^{-1}	Cycle number @ capacity / mAh g^{-1}	Ref
Nb-doped TiO_2 layer		100:00:00 1 M $NaClO_4$ in PC	0.005–3	C/7	300	50 @ 160	[7]
C-TiO_2-RN (nanorutile)	157	Mact:PVDF:Super-P 70:20:10 1 M $NaClO_4$ in EC: DEC 1:1	0.01–3	C/7, C/3, 1C	685.7	200 @ 138	[8]
N-TiO_2-RN (nanorutile)	117				599.7	200 @ 138	
Microspheres Anchored by Nanoneedle Cluster	49.2	Mact:SuperP:CMC 70:15:15 Celgard / 1 M $NaClO_4$ en PC:FEC 95:5	0.01–3	C/10	308.8	200 @ 121	[9]
Nanorods	180	Mact:acetylene Black:CMC 70:20:10 Slurry / 1 M $NaClO_4$ in EC:DEC 1:1	0.02–3	0.3C	487	170 @ 115	[10]
Mesocrystal	62	Mact:Super-P:PVDF 70:20:10 1 M $NaClO_4$ in EC: DEC 1:1	0.01–3	C/3	611	100 @ 283	[11]
Petals		Mact:CMC:Super-P 70:15:15 1 M $NaClO_4$ in PC: FEC 95:5	0.01–3	0.25C	337	300 @ 245	[12]
Rutile Cauliflower likeTiO_2 rutile (6.99 % Fe dopped)	53.15	Mact:PVDF:Super-P 70:20:10 1 M $NaClO_4$ in PC: FEC 95:5	0.01–3	C/2	550	50 @ 280	[13]
				2.5C	325	600 @ 186	
Ta-doped TiO_2 nanorods		Mact:acetylene Black:CMC: styrene-butadiene rubber 70:15:10:5 1 M NaFSA in PC	0.005–3	0.15C	290	300 @ >200	[14]
Nb-doped TiO_2 nanorods		Mact:acetylene Black:CMC: styrene-butadiene rubber 70:15:10:5 1 M NaFSA in PC	0.005–3	0.15C	~55	800 @ 200	[15]
Hollow TiO_2 Rutile Cuboid Arrays Grown on Carbon Fiber Cloth	103.5	100:0:0 1 M $NaClO_4$ in EC:DMC	0.01–3	C/10	388	100 @ 287	[16]
Hydrogenated Rutile TiO_2		Mact:carbonblack:PVDF 75:20:5 1 M $NaClO_4$ in EC:PC 1:1	0.01–2.5	1.5C (500 mA g^{-1})	~95	500 @ 95	[17]
Mooncake		Mact:ConductiveCarbon;PVDF 70:20:10 0.6 M $NaClO_4$ in EC:DEC 1:1	0.05–3	10C	109.5	1000 @ 132	[18]
Spherical	150	Mact:Ketjen Black:CMC: styrene-butadiene rubber 80:10:5:5 1 M $NaPF_6$ in DEG:DME	0.01–3	6C		3000 @ ~200	[19]

of solid mixture. The resulting slurry was cast onto a copper foil. Sodium metal (Panreac Quimica SLU) was used as the counter and reference electrode with Whatman GF/D glass fiber as the separator. The electrolyte used was 1 M $NaClO_4$ in 1:1 (v/v) ethylene carbonate (EC):propylene carbonate (PC). The electrochemical cells were assembled in an Ar-filled glove box (H_2O and O_2 <0.1 ppm).

The electrochemical performance of the TiO_2 nanorutile electrodes was evaluated by means of galvanostatic discharge-charge cycling at constant and variable current densities, cyclic voltammetry (CV), and electrochemical impedance spectroscopy (EIS). For galvanostatic discharge-charge cycling, cells were cycled at different current densities ranging from 17 mA g^{-1} (C/20) to 1678 mA g^{-1} (5C) in the potential range from open-circuit voltage (OCV) to 0.01 V vs. Na^+/Na to assess the sodium storage capacity and cycling stability. Specific capacity of all cells is given in mAh g^{-1} of active material (TiO_2) unless otherwise specified. Higher current rates (5C) were also applied to investigate the impact on capacity and rate performance, and the electrodes' ability to retain capacity when returning to the lower C/20 rate was monitored. Cyclic Voltammetry measurements were conducted at various potential sweep rates from low 0.009 mV s^{-1} to high 1.5 mV s^{-1} within a potential range of 2.8 to 0.01 V vs. Na^+/Na. This allowed the assessment of the faradic and surface (capacitive) contributions to charge storage under different cycling conditions, providing insights into the material's sodium storage mechanism. The contributions to the specific capacity of diffusion-controlled and surface processes were determined using the ratio between the current and the sweep rate, according to Eq. (1), and Wang et al. [22]:

$$I(\nu) = a\nu^b \tag{1}$$

that is rewritten for analytical purposes in Eq. (2) as:

$$I(\nu) = a_1\,\nu^1 + a_2\nu^{1/2} \tag{2}$$

and considering that the total current is the sum of current derived from two possible contributing charge storage mechanisms (capacitive, $b = 1$ and diffusion controlled, $b = 1/2$), according to a_1 and a_2 respectively, in Eq. (3) as:

$$I(\nu)/\nu^{1/2} = a_1\nu^{1/2} + a_2 \tag{3}$$

EIS measurements were performed during the first and fifth discharge cycles performed at 17 mA g^{-1} (C/20) to determine the sodium diffusion coefficient in TiO_2 nanorutile at different states of discharge at different specific potentials. The purpose of performing this experiment in the first and fifth cycle is to investigate possible changes that may occur during the first discharge, as in the case of lithium intercalation in TiO_2 rutile [20]. The sodium diffusion coefficient was calculated under conditions of semi-infinite diffusion according to Eq. (4): [23,24]

$$D_j = \left(\frac{V_m}{Z\,F\,SSA}\right)^2 \cdot \left(\frac{dE}{dx}\right)^2 \cdot \left(\frac{1}{m\,A_W\,\sqrt{2}}\right)^2 \tag{4}$$

V_m is the molar volume, Z the number of electrons per inserted ion, F the Faraday's constant, m the mass of the active material, and SSA the specific surface area of the electrode, as determined by BET and taken as the best approximation to effective intercalation surface. Galvanostatic experiments at 17 mA g^{-1} (C/20) were run to determine (dE/dx) at voltages where impedance measurements were done. Impedance spectroscopy was used to determine the Warburg coefficient (A_w) and its change upon reaction with sodium. Measurements were performed at OCV condition in a three-electrode cell and at several equilibrated voltages during the 1st and 5th discharge. The three-electrode cells allowed for the determination of the impedance response of the working electrode.

The in-situ XRD measurements were performed on a STOE Stadi-P diffractometer wit Ag-Kalpha1 source (λ = 0.559408 Å), Ge111 monochromator and Mythen-2 2 K detector. The sample setup [25], as well as the custom-made coin cells [26] are adapted for in-situ diffraction measurements. The X-ray transmitting holes of the coin cells are sealed with 50 μm Kapton foil. The working electrode was placed on a carbon cloth and the counter electrode was sodium-impregnated carbon fiber. The electrodes were separated by a WhatmannTM borosilicate separator which was impregnated with 1 M $NaClO_4$ in EC:PC (1:1) electrolyte. The cell was sealed in a cell press with a pressure of 650 psi.

3. Results and discussion

3.1. Structural and morphological characterization

Prolonged acidic treatment of a KTO bronze [17] in HCl:HNO_3 (1:3 v/v) at 80 °C produces rutile TiO_2 nanoneedles 4–5 nm wide and 50–100 nm long. XRD and TEM analyses confirm a tetragonal $P4_2/mnm$ crystal structure with anisotropic morphology, yielding aspect ratios of 10–15. Rietveld refinement indicates a well-ordered material with lattice parameters $a = b = 4.6044$ Å and $c = 2.9535$ Å (Fig. S1).

3.2. Electrochemical performance of TiO_2

The galvanostatic discharge-charge profile of nanorutile TiO_2 from an electrode using standard 8:1:1 wt % TiO_2, conductive carbon and CMC binder ratio, for the 1st, 2nd, 3rd, 50th and 100th cycles at a low current density (C/20, 17 mA g^{-1}), are shown in Fig. 1a. The TiO_2 electrode shows a 1st cycle discharge capacity of 381 mAh g^{-1}, equivalent to the insertion of 1.13 Na^+ ions/ f.u. of TiO_2, and a 1st charge capacity of 230 mAh g^{-1} (black curve), corresponding to 60 % of the first discharge capacity. The occurrence of irreversible capacity in the 1st

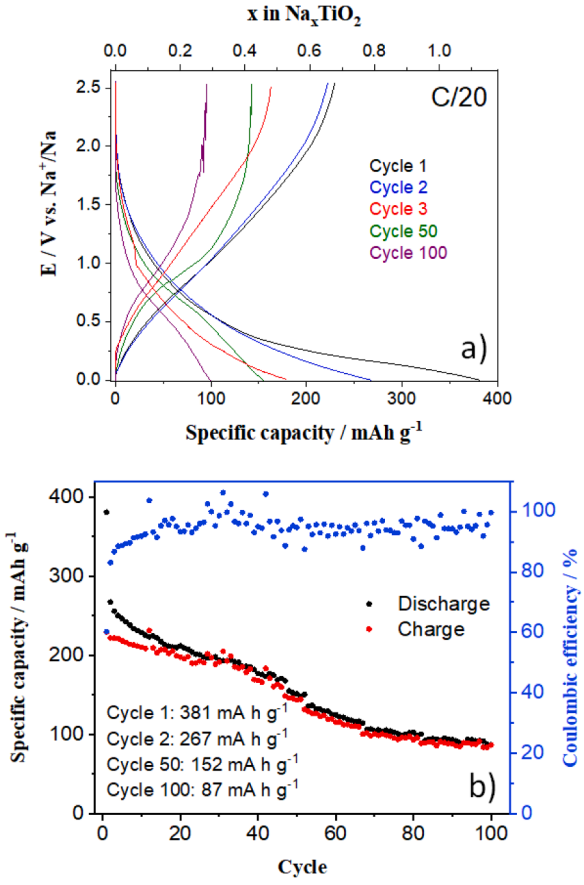

Fig. 1. Discharge-charge profile (a) and variation of capacity with cycle number (b) for TiO_2 vs. Na^+/Na at 17 mA g^{-1} (C/20).

cycle is a commonly observed feature in battery systems due to the formation of the solid electrolyte interphase (SEI) [27,28]. During SEI formation, sodium ions are irreversibly consumed. From cycle 50 onwards, the electrochemical profile presents instability at high voltage at the end of the charge process. This behavior may be a consequence of electrode degradation with increasing cycle number. The capacity of TiO_2 progressively decreases as cycle number increases (Fig. 1b) and Coulombic efficiency increases during the first 20 cycles approaching an average of ~ 97 %. The gradual decline in capacity suggests possible structural or chemical degradation of the electrode or the SEI/CEI layer during extended cycling. This degradation might result from electrolyte decomposition or volume expansion/contraction within the TiO_2 structure upon repeated Na^+ insertion and extraction. Exploring SEI stabilization strategies or the addition of protective layers could mitigate this capacity fading, thereby extending the material's cycle life. The initial capacity, once SEI/CEI is formed, is very competitive (> 225 mAh g^{-1}), and optimizing electrode manufacturing may lead to improved capacity retention.

The C-rate performance for TiO_2 at various current densities ranging between 17 mA g^{-1} (C/20) to 1678 mA g^{-1} (5C) is shown in Fig. 2. At low currents of 17 mA g^{-1} (C/20) and 34 mA g^{-1} (C/10), discharge and charge capacities differ, where discharge capacity of every cycle comes closer to charge capacity as the cycle number increases, indicating increasing stabilization of the SEI. For example, discharge capacities for the first three cycles at 17 mA g^{-1} are 351, 228 and 214 mAh g^{-1}, whereas the stable charge capacities are 183, 176 and 176 mAh g^{-1}. At high currents of 336 mA g^{-1} (1C) 672 mA g^{-1} (2C) and 1680 mA g^{-1} (5C), the TiO_2 electrode delivers 135 mAh g^{-1}, 115 mAh g^{-1}, and 71 mAh g^{-1}, highlighting its robust performance under fast charging and discharging conditions. After high-rate cycling, TiO_2 recovers its initial capacity when cycled at low 17 mA g^{-1} (C/20). This outstanding behavior could be related to the contribution of a fast charge/discharge mechanism, such as surface charge storage processes, and that needs to be investigated further. The capacitive nature of the TiO_2 material would allow rapid charge/discharge cycles without significant degradation. The high surface area of this TiO_2 nanorutile (77 m^2 g^{-1}) provides more accessible active sites for Na^+ adsorption, and the predominantly surface-controlled reactions may reduce the structural stress on the material during rapid cycling. Fig. 2 indicates that TiO_2 nanorutile exhibits very good C-rate performance at higher currents, and high stability of specific capacity and Coulombic efficiency are observed at currents above 34 mA g^{-1} (C/10). In contrast, at low current rate, redox intercalation may be favored, and electrode degradation is more likely as it can be deduced from Fig. 1b

To test this hypothesis, a TiO_2 vs. Na^+/Na cell was subjected to multiple discharge-charge cycles at a higher current of 67 mA g^{-1} (C/5), and the result is shown in Fig. 3. After the initial decrease in capacity from 246 mAh g^{-1} (cycle 1) to 108 mAh g^{-1} (cycle 6) due to SEI formation, TiO_2 exhibits excellent long-term cycling stability at the higher current rate of 67 mA g^{-1} (C/5) keeping a significant capacity of 140 mAh g^{-1}. The progressive increase in capacity from cycle 6 onwards could be attributed to electrochemical milling, as previously observed during Na intercalation in TiO_2(H) hollandite [29], to activation processes [30,31] or elimination of side reactions [7].

The SEM images of a pristine electrode before cycling, and post-mortem after 100 galvanostatic discharge-charge cycles at 67 mA g^{-1} (C/5) are shown in Fig. 4. Both the pristine electrode (Fig. 4a) and the electrode after 100 discharge-charge cycles (Fig. 4b) show very similar particle morphology, size and shape, which rules out electrochemical milling as the origin of the capacity increase at short number of cycles. The enhancement in electrochemical properties in anatase TiO_2 has been attributed to the boosted intrinsic electronic conductivity via metal reduction to lower valence states (Ti^{3+}) [32]. In our TiO_2 nanorutile, the slight discharge capacity overbalance (compared to charge capacity), derived from a small amount of intercalated sodium or surface redox pseudocapacitance, would originate lower valence Ti^{3+}, thus rendering enhanced electrochemical performance.

3.3. Charge storage mechanism in TiO_2

To understand the above presented electrochemical properties of the TiO_2 nanorutile electrode, CVs at different scan rates were carried out, specifically to determine the diffusion-controlled and capacitive contributions. Fig. 5 shows the voltammogram of TiO_2 at a low sweep rate of

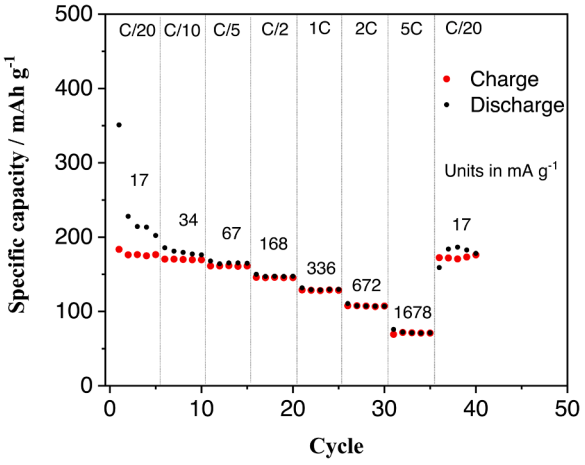

Fig. 2. Variation of specific capacity of TiO_2 vs. Na^+/Na at different successive C/n current rates (C/20–5C).

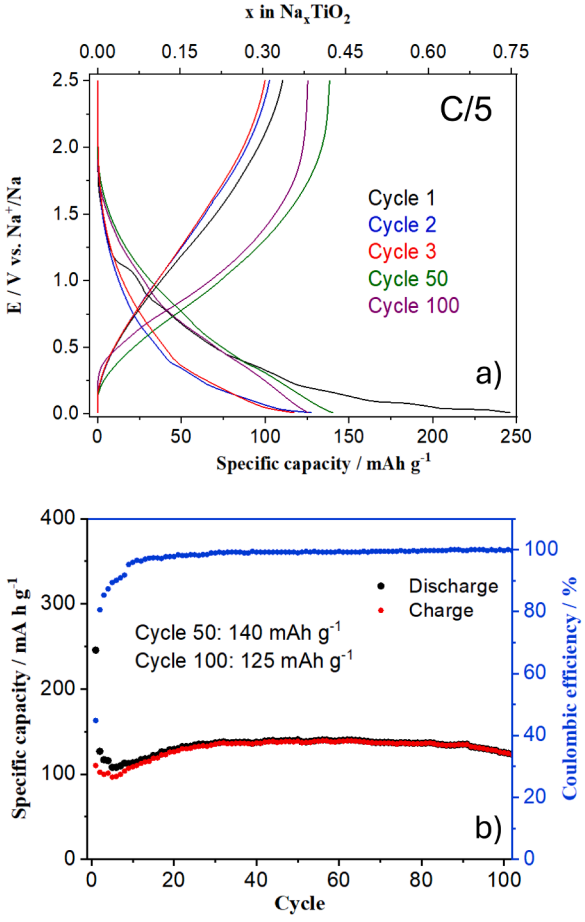

Fig. 3. Discharge-charge profile (a) and variation of capacity with cycle number (b) for TiO_2 vs. Na^+/Na at 67 mA g^{-1} (C/5).

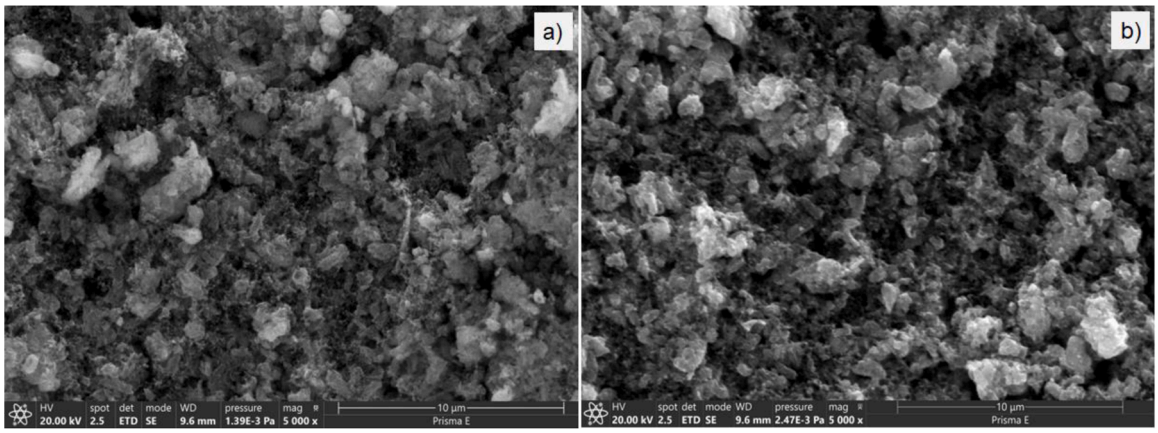

Fig. 4. SEM images of a TiO_2 based electrode (a) before discharge and (b) post-mortem after 100 discharge-charge cycles at 67 mA g^{-1} (C/5).

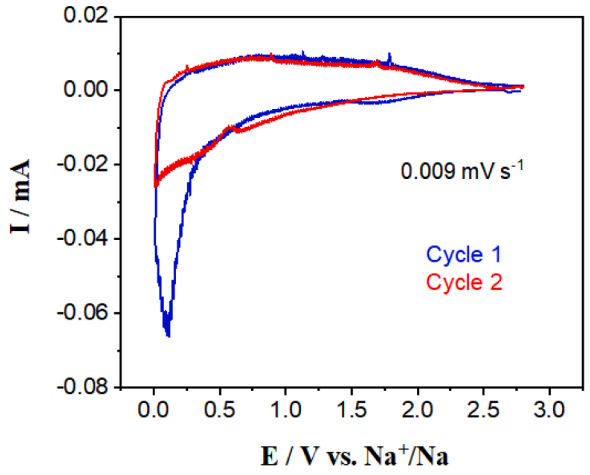

Fig. 5. Cyclic voltammetry of TiO_2 vs. Na^+/Na at 0.009 mV s^{-1} in the 2.7–0.01 V voltage range. The first two complete cycles are shown.

0.009 mV s^{-1}. The reduction peak detected at 0.2 V in the first cycle (blue line), which is not detected in consecutive cycles, may be attributed to electrolyte decomposition and SEI formation [9,12]. Fig. 6 shows the voltammograms after the 2nd cycle for sweep rates of 1.5, 1.2, 0.9, 0.6 and 0.3 mV s^{-1} (Fig. 6a) and 0.03, 0.02, 0.01 and 0.009 mV s^{-1} (Fig. 6b). In all cases, a reduction peak centered around 0.7 V is observed together with its homologous oxidation peak whose maximum is located close to 1.0 V. These redox signals are ascribed to the reversible Ti^{3+}/Ti^{4+} redox couple for the sodium insertion/extraction process [8, 12]. The profile of the CV after the first cycle is broad but with electrochemical reversible redox peaks pointing to pseudocapacitance behavior, likely surface redox pseudocapacitance [33].

Representing log (I) vs. log (ν), the value of the parameter 'b' in Eq. (1) can be deduced by calculating the slope of this relationship (Fig. S2). The values of 'b' obtained are close to 1. For example, in the charging stage, for a voltage of 2.3 V, $b = 0.75$; for 1 V, $b = 1.033$; and in the discharging stage, for 2.3 V, $b = 0.92$ and for 1 V, $b = 0.949$, which is interpreted as a high contribution of the above mentioned pseudocapacitive process to the overall charge storage in TiO_2.

According to Eq. (2), the current response at a given potential is influenced by the capacitive or diffusion-controlled mechanisms. The parameters a_1 (capacitive contribution) and a_2 (diffusion-controlled contribution) have been determined for each voltage value in the 2.7–0.01 V range by selecting points every 0.1 V. The data used for the calculation of these parameters are shown in Fig. S3, which shows selected values of a_1 and a_2 for each voltage for both charging and discharging state. After calculating the values a_1 and a_2, the equation $I(\nu) = a_1\nu + a_2\nu^{1/2}$ is applied. The result is the total current, which can be used to calculate the proportion corresponding to the capacitive ($a_1\nu$ / I (ν)) and faradaic ($a_2\nu^{1/2}$ / I (ν)) contribution. Multiplying the capacitive contribution by the value of the experimental intensity of the voltammograms allows the faradaic and capacitive contributions at each voltage to be identified graphically. As typical examples of both high and low sweep rates, Fig. 7a–d shows the distribution of the capacitive charge contribution (black color area) and the diffusion-controlled

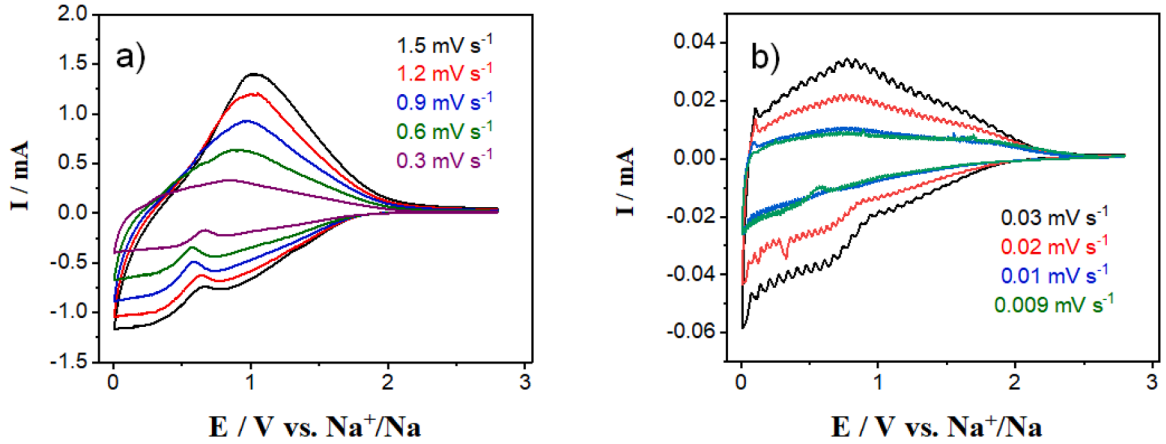

Fig. 6. Voltammograms of TiO_2 vs. Na^+/Na at different scan rates in the voltage range of 2.7–0.01 V at scan rates a) 1.5, 1.2, 0.9, 0.6, 0.3 mV s^{-1} and b) 0.03, 0.02, 0.01, 0.009 mV s^{-1}.

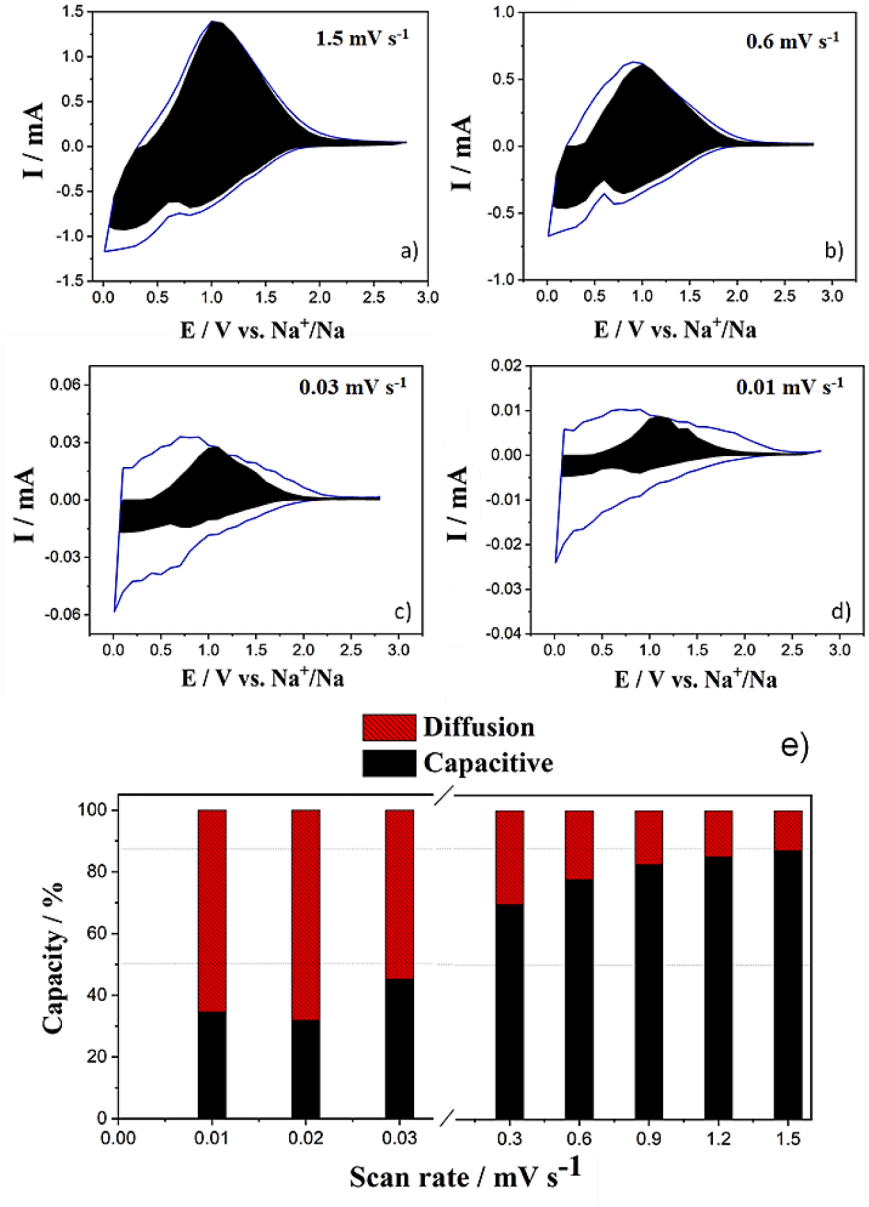

Fig. 7. Cyclic voltammetry at scan rates of a) 1.5 mV s^{-1}, b) 0.6 mV s^{-1}, c) 0.03 mV s^{-1}, d) 0.01 mV s^{-1}; e) Bar graph showing the percentage (%) of the capacitive and diffusion-controlled processes to the total capacity of TiO_2 as a function of scan rate in the range 0.009 - 1.5 mV s^{-1}.

contribution (white color area) to the total current for sweep rates of 1.5 mV s^{-1} (Fig. 7a), 0.6 mV s^{-1} (Fig. 7b), 0.03 mV s^{-1} (Fig. 7c) and 0.01 mV s^{-1} (Fig. 7d). At low sweep rates, such as 0.01 mV s^{-1}, the diffusion-controlled contribution is 65 %, confirming that at slow rates the Na^+ diffusion into the bulk is favored. In view of the CV profile shown in Fig. 6a, we have ascribed the capacitive contribution to pseudocapacitance, likely being surface redox pseudocapacitance. The pseudocapacitive contribution to the overall charge storage gradually increases as the sweep rate increases, from 34 % at 0.01 mV s^{-1} to 87 % at 1.5 mV s^{-1} (Fig. 7e). At a high sweep rate of 1.5 mV s^{-1}, the predominant contribution is pseudocapacitive (~87 %).

The fact that pseudocapacitive surface redox reactions proceed faster than diffusion-controlled processes without structural degradation and given the high percentage of capacitive contribution to overall charge storage in TiO_2, would explain the high stability of the capacity over a larger number of cycles at high rates [16].

3.4. *Sodium-ion diffusion kinetics in TiO_2*

In this work, the sodium diffusion coefficient, D^+_{Na}, was calculated from a combination of EIS and galvanostatic experiments analysis and considering BET surface area of TiO_2 (77.3 ± 0.8 m^2g^{-1}) as the effective area for sodium intercalation. In view of the result presented in Section 3.3, the EIS experiments were performed on cells discharged at low current to allow sodium intercalation to predominate over pseudocapacitance. Thus, a TiO_2 /Na cell bearing a third electrode (Na) as reference was discharged at 17 mA g^{-1} (C/20), and the impedance was determined in the 1st discharge at voltages of 2.2, 1.2, 1.0 V vs. Na^+/Na and in the 5th discharge at voltages of 1.6, 1.2 and 1.0 V vs. Na^+/Na. The sodium diffusion coefficient was determined according to Eq. (4) for which the Warburg coefficient was determined from EIS data and (dE/dx) from C/20 galvanostatic experiments for a more accurate determination of the thermodynamic factor.

Fig. 8 shows an exemplary Nyquist plot of the impedance response of the working electrode (80 % TiO_2) at 2.2 V in the first discharge using a

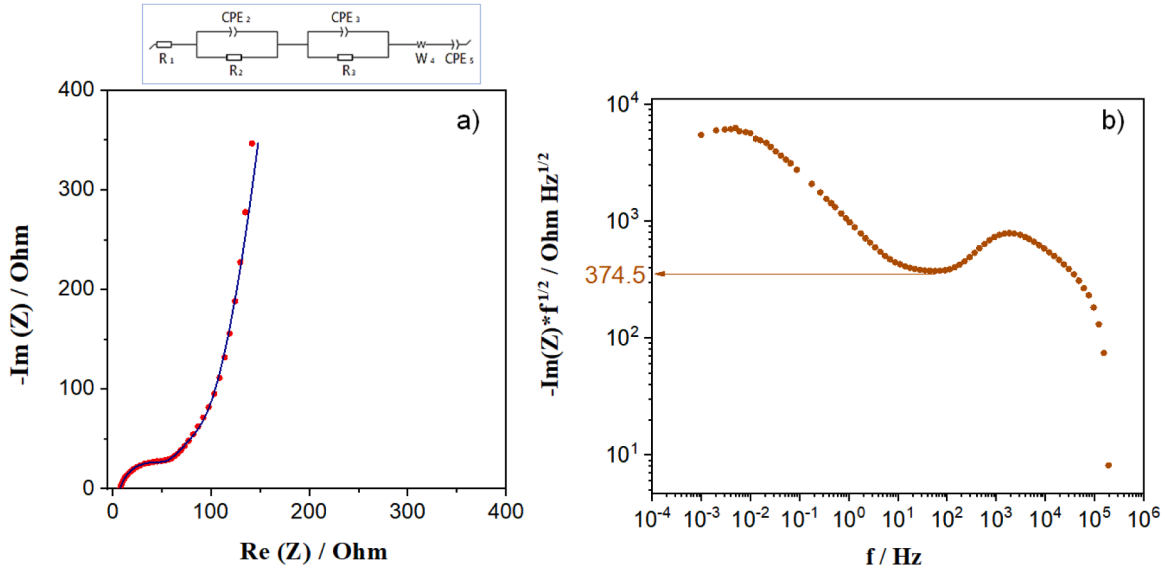

Fig. 8. a) Nyquist plot for the impedance of the working electrode TiO_2. The red dots correspond to the experimental data and the blue line corresponds to the fit obtained by equivalent circuit $R_1+R_2//CPE_2+ R_3//CPE_3+W_4+CPE_5$. b) Graphical determination of the Warburg coefficient, A_w, from the impedance data taken from a three-electrode cell in the first discharge at a potential of 2.2 V.

three-electrode cell (other examples of Nyquist graph at different voltages during the 1st and 5th discharge, see Figs. S4–S8). The Nyquist spectrum reveals the internal resistance of the cell: the electrolyte resistance (R_1) at high frequencies (low *Re* (Z) values); a semicircle at medium frequencies which is assigned to the charge transfer process (solvation/ desolvation and transfer of sodium ions to the interface) in parallel to the double layer capacitance and to the resistance and capacitance of CEI passivation layer ($R_2//CPE_2 + R_3//CPE_3$); Finally, at high frequencies, a spike related to the diffusion process modelled with a Warburg impedance is developed. The equivalent circuit shown in the inset at the top of Fig. 8a was used to fit the experimental data. The values of the Warburg coefficient, A_W, are determined from values for which $-Im(Z)*f^{1/2}$ remains constant vs. f (Fig. 8b). At low frequencies, the diffusion of charges within nanorutile TiO_2 gives rise to a Warburg impedance Z_W. At much lower frequency, the perturbation time is very long for small particles to have time enough to be fully sodiated even though the diffusion coefficient is very low. Thus, at such lower frequencies the finite thickness due to the nanosized nature of the nanorutile in combination with blocking at the interface, likely due to low diffusion coefficient, develops a capacitive behavior that deviates the phase angle from 45° toward 90° Thus, nanorutile is a typical case of finite length diffusion terminated with an interfacial capacitor [34,35]. The data from the galvanostatic experiment using a DC current density of 17 mA g^{-1}, corresponding to the 1st and the 5th discharge, were used to calculate the thermodynamic factor of Eq. (4) used to estimate the diffusion coefficients of Na^+ in TiO_2. The sodium diffusion coefficient into TiO_2 is found to range from $4.2 \cdot 10^{-17}$ cm^2 s^{-1} at 1.2 V to $3.1 \cdot 10^{-17}$ cm^2 s^{-1} at 1 V in the 1st discharge, and from $2.5 \cdot 10^{-17}$ cm^2 s^{-1} at 1.6 V to $1.7 \cdot 10^{-16}$ cm^2 s^{-1} at 1.0 V in the 5th discharge (see Table 2).

It is then confirmed that the Na^+ diffusion coefficient in TiO_2 is low, as one may expect because the diffusion of Na^+ ions with 204 pm in size along the rutile *c*-axis, with a tunnel width of 230 pm, would be somehow inhibited [36]. This agrees with the predominant capacitive contribution to overall charge storage at high sweep rate, as determined by cyclic voltammetry. However, the sodium diffusion coefficient in the herein presented rod-shaped TiO_2 nanorutile is several orders of magnitude higher compared with the Na^+ diffusion coefficient in TiO_2 rutile of $1.35 \cdot 10^{-20}$ cm^2 s^{-1} [37] determined by Ghosh *et al.* The Na^+ diffusion coefficients for different TiO_2 polymorphs, including that of the present work, are compared in Table 3.

On the other hand, the diffusion coefficient D^+_{Na} in TiO_2 nanorutile is clearly lower when compared to the Na^+ diffusion coefficient in TiO_2 hollandite (10^{-13} cm^2 s^{-1}) [29]. This is reasonable because the 2 × 2 channels in the hollandite structure (670.7 pm) [41] through which sodium diffuses are significantly larger than the 1 × 1 channels in rutile (230 pm) [36]. It is also worth mentioning that lithium diffusion coefficient D^+_{Li} into rutile TiO_2 nanorods was found to be 10^{-16} - 10^{-15} cm^2 s^{-1} [20], a signature of the smaller lithium ion, with 152 pm in size significantly smaller than the sodium ion, and which enables better ion diffusion through the channels in rutile [36].

3.5. *Effect of additional conductive carbon on the electrochemical performance of TiO_2*

To improve the performance of TiO_2 nanorutile as anode in SIBs, electrodes with an increased conductive carbon content were employed to attenuate their insulating characteristics and enhance electronic conductivity of the composite. Based on the satisfactory results in our previous work on sodium intercalation in TiO_2 hollandite, electrodes with a 6.5:2.5:1 wt % of active material, conductive carbon and binder

Table 2
Sodium diffusion coefficients in TiO_2 determined in the 1st and 5th discharge at different voltages.

Discharge	E / V	D^+_{Na}/ cm^2s^{-1}	x in Na_xTiO_2
1	1.2	$4.2 \cdot 10^{-17}$	0.2982
1	1	$3.1 \cdot 10^{-17}$	0.3478
5	1.6	$2.5 \cdot 10^{-17}$	0.02483
5	1.2	$1.9 \cdot 10^{-16}$	0.1242
5	1	$1.7 \cdot 10^{-16}$	0.5463

Table 3
Sodium diffusion coefficients of different TiO_2 polymorphs calculated by EIS.

	Polymorph	D^+_{Na} / cm^2s^{-1}	Ref.
TiO_2	Hollandite	$2.60 \cdot 10^{-13}$	[29]
	Rutile	$2.5 \cdot 10^{-17}$ - $1.90 \cdot 10^{-16}$	This work
	Rutile	$1.35 \cdot 10^{-20}$	[37]
	Anatase	$7.60 \cdot 10^{-15}$	[38]
	Anatase	$5.50 \cdot 10^{-13}$	[39]
	Anatase	$7.02 \cdot 10^{-13}$	[40]

were specifically used. The use of an increased conductive carbon content is a common practice in electrically insulating materials [7,42–45].

For clarity, electrodes with 8:1:1 ratio are labelled 80-TiO_2-r, while conductive carbon-enriched electrodes with 6.5:2.5:1 ratio are labelled 65-TiO_2-r. Fig. 9 shows the excellent cycling stability of both 80-TiO_2-r and 65-TiO_2-r. 1st discharge capacities at a low current of 34 mA g^{-1} (C/10) are 374 mAh g^{-1} and 269 mAh g^{-1}, respectively, while CE, due to SEI formation, remains almost unaltered (43 % and 48 % respectively, see Fig. S9). Fig. S9 shows that both the 1st discharge capacity of 65-TiO_2-r (374 mAh g^{-1}) and that delivered in subsequent cycles (165–170 mAh g^{-1}) are systematically higher compared to 80-TiO_2-r. The capacity of carbon-rich 65-TiO_2-r is higher than that of 80-TiO_2-r, referred to both mass of active TiO_2 (Fig. 9a) and total mass of electrode (Fig. 9b), being up to 23.5 % higher when referred to mass of active material.

The C-rate performance of both 80-TiO_2-r and 65-TiO_2-r at various current densities ranging from 17 mA g^{-1} (C/20) to 1678 mA g^{-1} (5C) are shown in Fig. 10. It can be seen that carbon-enriched 65-TiO_2-r delivers up to 80 % higher capacity than 80-TiO_2-r between 17 mA g^{-1} and 1678 mA g^{-1}. At low currents of 17 mA g^{-1} (C/20), 34 mA g^{-1} (C/10) and 67 mA g^{-1} (C/5), 65-TiO_2-r delivers capacities of 280 mAh g^{-1}, 230 mAh g^{-1}, 200 mAh g^{-1}, compared to 210 mAh g^{-1}, 180 mAh g^{-1}, 170 mAh g^{-1} for 80-TiO_2-r for the same current densities. At high currents of 336 mA g^{-1} (1C), 672 mA g^{-1} (2C), 1678 mA g^{-1} (5C), 65-TiO_2-r delivers a stable capacity of 128 mAh g^{-1} without signs of deterioration, whereas 80-TiO_2-r develops poorer capacity. It keeps 128 mAh g^{-1} at 336 mA g^{-1} (1C), but unlike 65-TiO_2-r, capacity strongly drops at higher currents of 672 mA g^{-1} (2C) and 1678 mA g^{-1} (5C) to 107 mAh g^{-1} and 71 mAh g^{-1}, respectively. After high rate cycling both 80-TiO_2-r and 65-TiO_2-r materials retain their initial capacities when cycled at low 17 mA g^{-1}, with a higher capacity in carbon-enriched 65-TiO_2-r. It is clear that the enhanced C-rate performance with high-capacity retention, especially at high current, is due to the enhanced conductivity of the composite. Thus, it has been demonstrated that the electrochemical performance of carbon-enriched TiO_2 electrodes (6.5:2.5:1 wt %) are significantly improved compared to standard TiO_2 electrodes (8:1:1 wt %) in terms of specific capacity, referred to either active mass or total mass of electrode, C-rate performance, and charge-discharge cycling.

3.6. Structural effects of sodium insertion in TiO_2 nanorutile

Ex-situ X-ray diffraction patterns of the TiO_2 anode after the 1st, 4th and 5th full discharge-charge cycles (Fig. S10) performed at 17 mA g^{-1} (C/20) are fully indexed with the tetragonal rutile structure in space group $P4_2/mnm$, with negligible changes in peak positions and intensities, evidencing that the rutile structure remains unaltered *after*

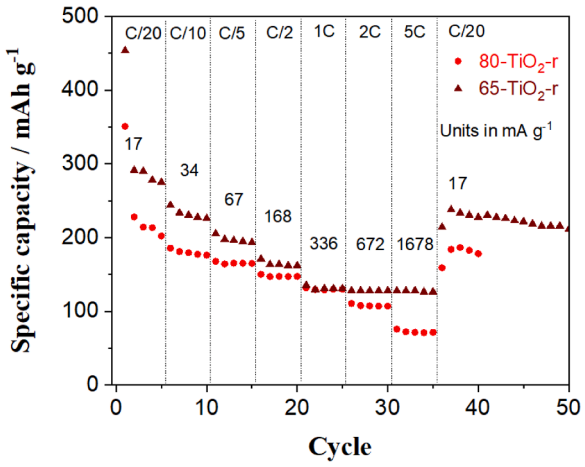

Fig. 10. Variation of the specific capacity of 80-TiO_2-r and 65-TiO_2-r at increasing current intensities C/n (C/20–5C).

slow cycling. The atomic structure of rutile TiO_2 nanorods was further investigated with TEM (Fig. 11). The TEM images reveal the lattice fringes of pristine TiO_2 (Fig. 11a and b) and after 100 discharge-charge cycles (Fig. 11d and e) at 34 mA g^{-1} (C/10). The TiO_2 nanorods evolve along the [001] tunnel direction with (001) crystal plane spacings of 0.295 nm perpendicular to the (110) crystal planes of 0.330 nm (Fig. 11a). The post-mortem electrode (Fig. 11b) consists of TiO_2 highly agglomerated with the conductive carbon and shows spacings of 0.340 nm corresponding to the (110) crystal planes of TiO_2. The SAED patterns of both uncycled TiO_2 (Fig. 9c) and after 100 cycles (Fig. 11f) at 34 mA g^{-1} (C/10) were fully indexed with the tetragonal rutile structure, impressively confirming the robustness of the rutile structure upon cycling, consistent with ex-situ XRD (Fig. S2) and TEM (Fig. 11a and d).

Operando XRD was collected for two electrode samples, 80-TiO_2-r with regular conductive carbon content, and conductive carbon-enriched 65-TiO_2-r, to assess the structural changes associated with sodiation and desodiation. Fig. 12a shows the in-situ XRD patterns of 80-TiO_2-r and the corresponding sodiation and desodiation curves (Fig. 12b) collected during two cycles at slow 17 mA g^{-1} (C/20), followed by two cycles at faster 67 mA g^{-1} (C/5) and finally two cycles at 17 mA g^{-1}. Remarkably, the characteristic TiO_2 reflections - (110), (111), (121), (002), etc. - are continuously shifted toward lower angles throughout the first discharge (sodiation) at 17 mA g^{-1} in the 3.0–0.01 V vs. Na^+/Na range, indicating the formation of a single-phase Na_xTiO_2 solid solution. Interestingly, during the first charge a continuous

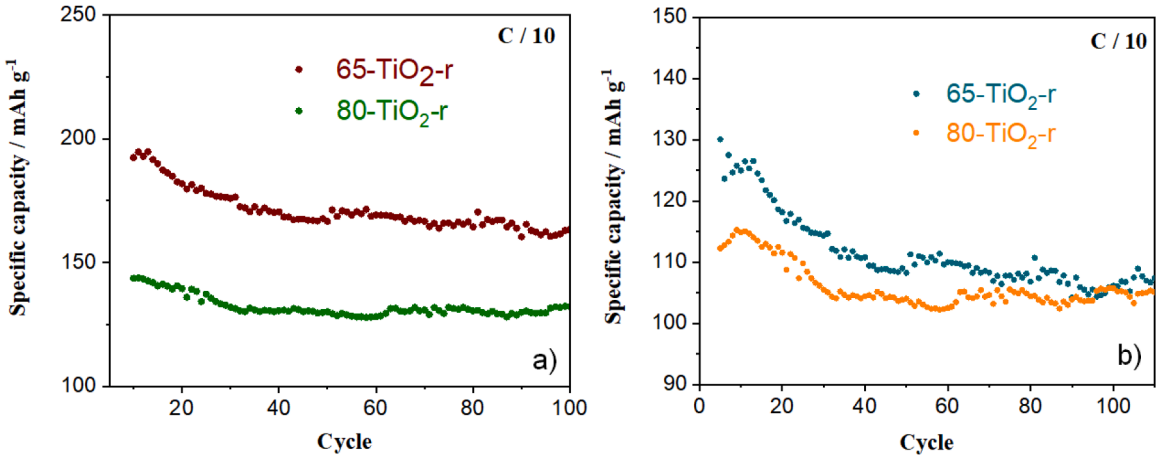

Fig. 9. Variation of capacity of 65-TiO_2-r vs. Na^+/Na and 80-TiO_2-r vs. Na^+/Na with the number of cycles at 34 mA g^{-1} (C/10), per a) mass of active material and b) total mass of electrode.

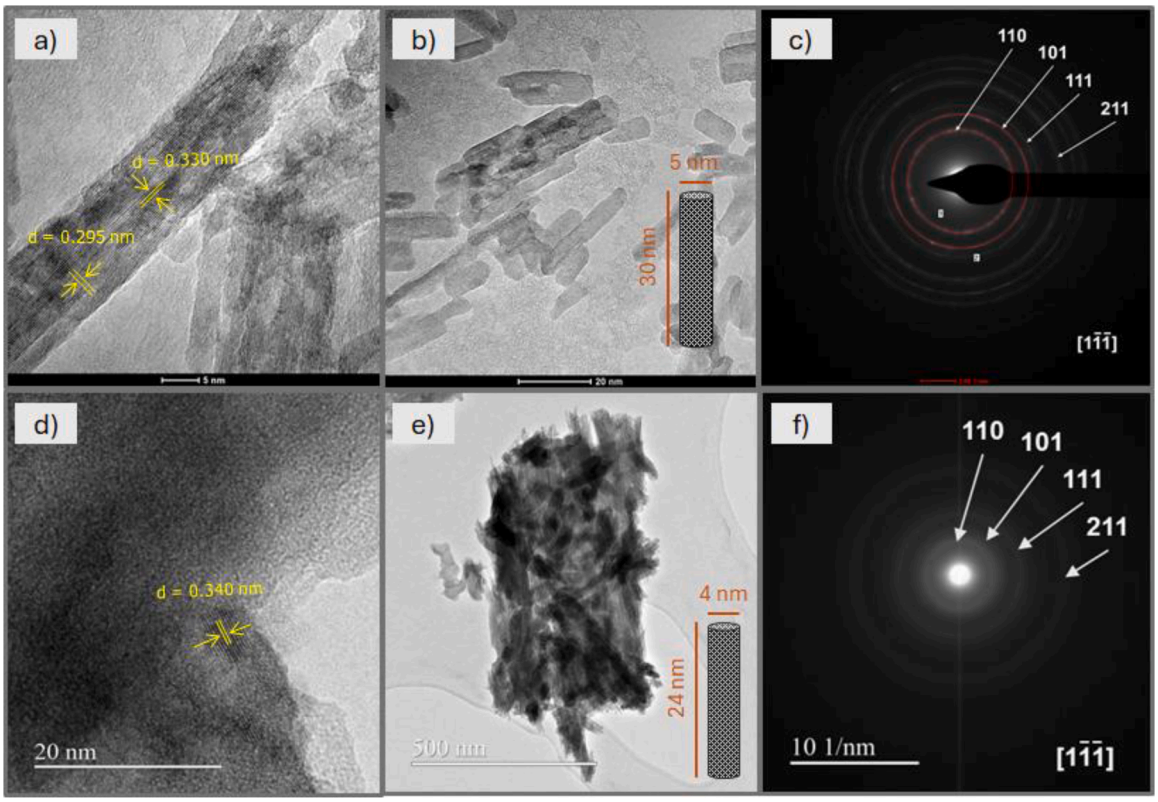

Fig. 11. TEM images of TiO_2-r (a-c) before and (d-f) after 100 cycles at 34 mA g^{-1} (C/10) in the voltage range 2.7–0.01 V vs. Na^+/Na.

retrogression of all reflections occurs, confirming the reversibility of the sodium intercalation-deintercalation mechanism, which is also maintained in successive cycles (as deduced from reversible shift of TiO_2 reflections during subsequent cycling). The evolution of characteristic cell parameters (*a, c* and volume), as deduced from Rietveld refinement, during cycling is portrayed in Fig. 12c. Lattice parameters *a* and *c* increase anisotropically during successive sodiation cycles ($\Delta a/a = +2.1$ %, $\Delta c/c = +0.5$ %, $\Delta V/V = +4.8$ % in the first discharge), with a more pronounced increase in *a* (which reflects the width of the approximately square tunnel) to better accommodate the intercalated Na^+ ions. Cycling at a higher C-rate of 67 mA g^{-1} is associated with less pronounced shifts of reflections, anticipating attenuated structural changes. This differential C-rate dependent behavior reflects the more pronounced faradic character (sodium intercalation) of TiO_2 at low current density, while pseudo-capacitive surface sodium storage takes control at high-rate cycling.

Fig. S11a shows the in-situ XRD patterns of conductive carbon-enriched 65-TiO_2-r together with the corresponding sodiation and desodiation curves (Fig. S11b) collected during two cycles at slow 17 mA g^{-1} (C/20), followed by two cycles at faster 67 mA g^{-1} (C/5) and finally two cycles at 17 mA g^{-1}. As already observed before in 80-TiO2-r, 65-TiO2-r shows the same reversible continuous shift of the characteristic TiO_2 rutile reflections during successive sodiation and desodiation cycles (Fig. S11a), with formation of single-phase Na_xTiO_2 solid solution. However, remarkably, in 65-TiO2-r the diffraction peaks shift more strongly compared to 80-TiO2-r, associated with larger reversible variation in the rutile cell parameters. This suggests that the enhanced electronic conductivity in carbon-enriched 65-TiO2-r enables enhanced Na^+ ion intercalation in the rutile tunnels, favoring superior electrochemical performance of 65-TiO2-r compared to 80-TiO2-r as discussed above.

4. Conclusion

In summary, electrochemical performance of TiO_2 rutile nanorods has been evaluated. After SEI formation it exhibits an initial discharge capacity of ~260 mAh g^{-1}, stabilizing at 140 mAh g^{-1} after 100 cycles. Its robust performance at high current densities, such as 164 mAh g^{-1} (C/5), highlights its viability as a negative electrode for sodium-ion batteries. The sodium diffusion coefficient $D^+_{Na} \approx 10^{-16}$–$10^{-17}$ cm^2 s^{-1}), determined in this work, anticipates a limited diffusion in such 1 × 1 tunnel structure, compared with that of the 2 × 2 tunnel structure of TiO_2 hollandite.

Moreover, the nanorutile TiO_2 demonstrated high electrochemical performance for sodium-ion storage, with the optimized wt.- % ratio of 6.5:2.5:1 delivering a higher capacity to total mass ratio, enhanced rate capability and cycle stability. Increasing conductive carbon content notably improves the electrochemical performance of TiO_2, enhancing conductivity and reducing cell polarization. The carbon-enriched electrode composition results in a 40 mAh g^{-1} higher reversible capacity (+23.5 %), which proves its impact in the optimization of electrode performance. Sodium intercalation in the tunnels of rutile TiO_2, as proven for the first time by *operando* X-ray diffraction and ex-situ TEM, significantly contributes to Na-ion storage at low-rate, further enhanced using conductive carbon-enriched TiO_2 electrodes, providing additional electrochemical performance.

The low Na^+ diffusion coefficient along the tunnel *c*-axis is consistent with the large size of Na^+ ions, which may lead to loss of capacity and structural deformation at lower currents due to prolonged ion diffusion. On the other hand, higher current densities (e.g., C/10 or C/5) promote capacitive processes, resulting in stable capacity retention over a large number of cycles at high rate. Cyclic voltammetry revealed that surface redox processes significantly contribute to the total specific capacity, ranging from 34 % at 0.01 mV s^{-1} to 87 % at 1.5 mV s^{-1}, consistent with the limited Na^+ diffusion in TiO_2 rutile. Finally, this study underlines the importance of electrode composition and the specific surface area of the

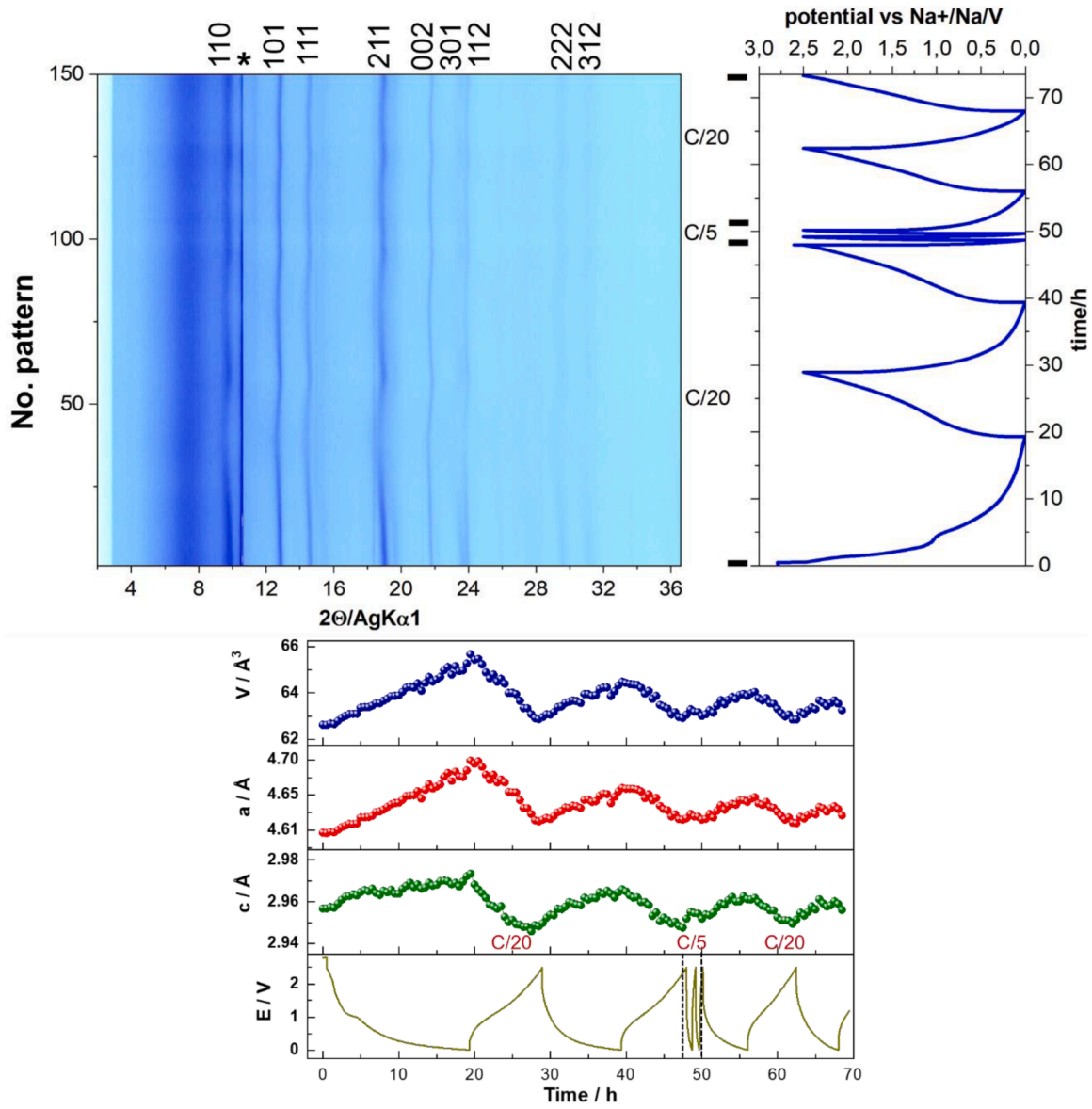

Fig. 12. Structure evolution of 80-TiO_2-r upon sodiation and desodiation. In-situ XRD patterns (a) and corresponding sodiation (discharge) and desodiation (charge) curves at 17 mA g^{-1} (C/20), 67 mA g^{-1} (C/5) and 17 mA g^{-1} with two full cycles at each current density (b). Reflection from Na anode is labelled with *. Corresponding variation of cell parameters upon cycling (c).

active material in improving electrochemical properties of rutile TiO_2, supporting its potential for high-performance sodium-ion battery applications.

CRediT authorship contribution statement

Angélica Duarte-Cárdenas: Investigation, Formal analysis, Methodology, Writing – original draft. **Liuda Mereacre:** Investigation, Formal analysis, Methodology, Validation. **Michael Knapp:** Formal analysis, Methodology, Validation, Writing – review & editing. **Pilar Díaz-Carrasco:** Investigation, Methodology, Validation, Writing – review & editing. **Flaviano García-Alvarado:** Investigation, Conceptualization, Writing – review & editing, Funding acquisition. **Alois Kuhn:** Investigation, Conceptualization, Supervision, Writing – review & editing, Funding acquisition.

Declaration of competing interest

The authors declare the following financial interests/personal relationships which may be considered as potential competing interests:

Alois Kuhn reports financial support was provided by Spain Ministry of Science and Innovation and EU Next Generation/PRTR. Flaviano Garcia-Alvarado reports financial support was provided by Spain Ministry of Science and Innovation and FEDER,UE. Angelica Duarte-Cardenas reports financial support was provided by Community of Madrid. If there are other authors, they declare that they have no known competing financial interests or personal relationships that could have appeared to influence the work reported in this paper.

Acknowledgments

This work has been supported by the Spanish projects PID2022-139039OB-C21 funded by MCIN/AEI/10.13039/501100011033/ FEDER,UE and TED2021-129427B-I00 funded by AEI/10.13039/ 501100011033/ Unión Europea Next Generation EU/PRTR. A.D.C. thanks Community of Madrid for granting the research contract PEJ-2017-AI/IND-6803. Support from Universidad San Pablo-CEU is acknowledged. We thank Prof. Mª José-Torralvo Fernández, Universidad Complutense Madrid, for the BET measurements. We thank ICTS-CNME for electron microscopy facilities and technical support.

Supplementary materials

Supplementary material associated with this article can be found, in the online version, at doi:10.1016/j.electacta.2025.146113.

References

[1] L. Fu, et al., Nitrogen doped porous carbon fibres as anode materials for sodium ion batteries with excellent rate performance, Nanoscale 6 (2014) 1384–1389.
[2] N. Sun, H. Liu, B. Xu, Facile synthesis of high performance hard carbon anode materials for sodium ion batteries, J. Mater. Chem. A Mater. 3 (2015) 20560–20566.
[3] Y. Cao, et al., Sodium ion insertion in hollow carbon nanowires for battery applications, Nano Lett. 12 (2012) 3783–3787.
[4] J. Jamnik, J. Maier, Nanocrystallinity effects in lithium battery materials: aspects of nano-ionics. Part IV, Phys. Chem. Chem. Phys. 5 (2003) 5215–5220.
[5] I. Hasa, J. Hassoun, S. Passerini, Nanostructured Na-ion and Li-ion anodes for battery application: a comparative overview, Nano Res. 10 (2017) 3942–3969, https://doi.org/10.1007/s12274-017-1513-7. Preprint at.
[6] M.B. Vazquez-Santos, P. Tartaj, E. Morales, J.M. Amarilla, TiO2 Nanostructures as anode materials for Li/Na-ion batteries, Chem. Record. 18 (2018) 1178–1191.
[7] H. Usui, S. Yoshioka, K. Wasada, M. Shimizu, H. Sakaguchi, Nb-doped rutile TiO_2: a potential anode material for Na-ion battery, ACS Appl. Mater. Interface. 7 (2015) 6567–6573.
[8] Z. Hong, K. Zhou, J. Zhang, Z. Huang, M. Wei, Facile synthesis of rutile TiO_2 mesocrystals with enhanced sodium storage properties, J. Mater. Chem. A 3 (2015) 10715–10722.
[9] Z. Y, et al., An electrochemical investigation of rutile TiO_2 microspheres anchored by nanoneedle clusters for its sodium storage, Phys. Chem. Chem. Phys. 3 (2015) 10715–10722.
[10] X. Gu, et al., Hierarchical tubular structures constructed from rutile TiO_2 nanorods with superior sodium storage properties, Electrochim. Acta 211 (2016) 77–82.
[11] Z. Hong, J. Hong, C. Xie, Z. Huang, M. Wei, Hierarchical rutile TiO_2 with mesocrystalline structure for Li-ion and Na-ion storage, Electrochim. Acta 202 (2016) 203–208.
[12] Y. Zhang, et al., Graphene-rich wrapped petal-like rutile TiO_2 tuned by carbon dots for high-performance sodium storage, Adv. Mater. 28 (2016) 9391–9399.
[13] H. He, et al., Iron-doped cauliflower-like rutile TiO2 with superior sodium storage properties, ACS Appl. Mater. Interface. 9 (2017) 6093–6103.
[14] H. Usui, Y. Domi, K. Takama, Y. Tanaka, H. Sakaguchi, Tantalum-doped titanium oxide with rutile structure as a novel anode material for sodium-ion battery, ACS Appl. Energy Mater. 2 (2019) 3056–3060.
[15] H. Usui, Y. Domi, S. Ohnishi, H. Sakaguchi, Single-crystalline Nb-doped rutile TiO_2 nanoparticles as anode materials for Na-ion batteries, ACS Appl. Nano Mater. 2 (2019) 5360–5364.
[16] C. Wang, J. Zhang, X. Wang, C. Lin, X.S. Zhao, Hollow rutile cuboid arrays grown on carbon Fiber cloth as a flexible electrode for sodium-ion batteries, Adv. Funct. Mater. 30 (2020) 1–10.
[17] J. Patra, et al., Hydrogenated anatase and rutile TiO2for sodium-ion battery anodes, ACS Appl. Energy Mater. 4 (2021) 5738–5746.
[18] G. Liu, et al., Metal-organic frameworks derived anatase/rutile heterostructures with enhanced reaction kinetics for lithium and sodium storage, Chem. Eng. J. 430 (2022) 132689.
[19] Z. Yan, et al., Unifying electrochemically-driven multistep phase transformations of rutile TiO2 to rocksalt nanograins for reversible Li+ and Na+ storage, Adv. Mater. 2419999 (2025) 1–9.
[20] P. Díaz-Carrasco, A. Duarte-Cárdenas, A. Kuhn, F. García-Alvarado, Understanding the high performance of nanosized rutile TiO_2 anode for lithium-ion batteries, J. Power Source. 515 (2021) 1–11.
[21] J.C. Pérez-Flores, C. Baehtz, A. Kuhn, F. García-Alvarado, Hollandite-type TiO2: a new negative electrode material for sodium-ion batteries, J. Mater. Chem. A Mater. 2 (2014) 1825–1833.
[22] J. Wang, J. Polleux, J. Lim, B. Dunn, Pseudocapacitive contributions to electrochemical energy storage in TiO_2 (anatase) nanoparticles, J. Phys. Chem. C 111 (2007) 14925–14931.
[23] W. Weppner, R.A. Huggins, Determination of the kinetic parameters of mixed-conducting electrodes and application to the system LLSb, J. Res. Nat. Bur. Stand., Sect. A 124 (1962).
[24] C. Ho, I.D. Raistrick, R.A. Huggins, Application of A-C techniques to the study of lithium diffusion in tungsten trioxide thin films, J. Electrochem. Soc. 127 (1980) 343–350.
[25] P. Sharma, et al., Synthesis and characterization of a multication doped Mn spinel, $LiNi_{0.3}Cu_{0.1}Fe_{0.2}Mn_{1.4}O_4$, as 5 v positive electrode material, ACS Omega 5 (2020) 22861–22873.
[26] Home – KIT – Campus transfer. https://kit-campus-transfer.de/en/home/.
[27] S.M. Oh, et al., High electrochemical performances of microsphere C-TiO_2 anode for sodium-ion battery, ACS Appl. Mater. Interface. 6 (2014) 11295–11301.
[28] R. Wu, et al., Soft-templated self-assembly of mesoporous anatase TiO_2/carbon composite nanospheres for high-performance lithium ion batteries, ACS Appl. Mater. Interface. 8 (2016) 19968–19978.
[29] A. Duarte-Cárdenas, P. Díaz-Carrasco, A. Kuhn, A. Basa, F. García-Alvarado, Deepening into the charge storage mechanisms and electrochemical performance of TiO_2 hollandite for sodium-ion batteries, Electrochim. Acta 427 (2022).
[30] L. Wu, D. Buchholz, D. Bresser, L. Gomes Chagas, S. Passerini, Anatase TiO_2 nanoparticles for high power sodium-ion anodes, J. Power Source. 251 (2014) 379–385.
[31] X. Yang, et al., Anatase TiO_2 nanocubes for fast and durable sodium ion battery anodes, J. Mater. Chem. A Mater. 3 (2015) 8800–8807.
[32] J. Chen, et al., Black anatase titania with ultrafast sodium-storage performances stimulated by oxygen vacancies, ACS Appl. Mater. Interface. 8 (2016) 9142–9151.
[33] Y. Gogotsi, R.M. Penner, Energy storage in nanomaterials - capacitive, pseudocapacitive, or battery-like? ACS Nano 12 (2018) 2081–2083.
[34] A. Lasia, Electrochemical Impedance Spectroscopy and Its Applications, Springer, Sherbrooke, Québec, 2014, https://doi.org/10.1007/978-1-4614-8933-7.
[35] B.A. Boukamp, A Nonlinear Least Squares Fit Procedure for Analysis of Immittance Data of Electrochemical Systems, 1986, https://doi.org/10.1016/0167-2738(86)90031-7. https://www.sciencedirect.com/science/article/pii/0167273886900317.
[36] H. Usui, Y. Domi, H. Sakaguchi, Rutile TiO2 creates advanced Na-storage materials, ACS Appl. Energy Mater. 6 (2023) 4089–4102.
[37] S. Ghosh, V. Kiran Kumar, S.K. Kumar, S. Biswas, S.K. Martha, An insight of sodium-ion storage, diffusivity into TiO_2 nanoparticles and practical realization to sodium-ion full cell, Electrochim. Acta 316 (2019) 69–78.
[38] X. Wang, L. Qi, H. Wang, Anatase TiO2 as a Na+-storage anode active material for dual-ion batteries, ACS Appl. Mater. Interface. 11 (2019) 30453–30459.
[39] L. Ling, et al., Remarkable effect of sodium alginate aqueous binder on anatase TiO_2 as high-performance anode in sodium ion batteries, ACS Appl. Mater. Interface. 10 (2018) 5560–5568.
[40] X. Ma, J.L. Tian, F. Zhao, J. Yang, B.F. Wang, Conductive TiN thin layer-coated nitrogen-doped anatase TiO_2 as high-performance anode materials for sodium-ion batteries, Ion. (Kiel) 24 (2018) 3771–3779.
[41] D. Li, et al., Tunnel structured hollandite $K_{0.06}TiO_2$ microrods as the negative electrode for 2.4 V flexible all-solid-state asymmetric supercapacitors with high performance, J. Power Source. 413 (2019) 34–41.
[42] J.T. Han, Y.H. Huang, J.B. Goodenough, New anode framework for rechargeable lithium batteries, Chem. Mater. 23 (2011) 2027–2029.
[43] H. Song, Y.-T. Kim, A Mo-doped $TiNb_2O_7$ Anode for Lithium-Ion Batteries with High Rate Capability due to Charge Redistribution, Chemical Communications, 2015 in vols 2019-November 9849–9852.
[44] H. Li, et al., TiNb2O7 nanoparticles assembled into hierarchical microspheres as high-rate capability and long-cycle-life anode materials for lithium ion batteries, Nanoscale 7 (2015) 619–624.
[45] R. Inada, et al., Characterization of vacuum-annealed TiNb2O7 as high potential anode material for lithium-ion battery, Int. J. Appl. Ceram. Technol. 16 (2019) 264–272.